Methylamine gas treatment affords improving semi-transparency, efficiency and stability of CH3NH3PbBr3-based perovskite solar cells

Ajay Singh, Fabio Matteocci, Hongwei Zhu, Daniele Rossi, Salim Mejaouri, Stefania Cacovich, Matthias auf Der Maur, Frédéric Sauvage, Alessio Gagliardi, Michael Grätzel, et al.

Methylamine gas treatment affords improving semi-transparency, efficiency and stability of $CH_3NH_3PbBr_3$-based perovskite solar cells

Ajay Singh[1, #], Fabio Matteocci[2, #], Hongwei Zhu[3], Daniele Rossi[2], Salim Mejaouri[4,5], Stefania Cacovich[4,6], Matthias Auf Der Maur[2], Frédéric Sauvage[7], Alessio Gagliardi[1] Michael Grätzel[3] and Aldo Di Carlo[2,*]

[1]Department of Electrical and Computer Engineering, Technical University of Munich, Karlstraße 45, 80333 Munich, Germany

[2]CHOSE (Centre for Hybrid and Organic Solar Energy), Department of Electronic Engineering, University of Rome "Tor Vergata", 00133, Rome, Italy

[3]Laboratory of Photonics and Interfaces (LPI) Ecole Polytechnique Fédérale de Lausanne, CH-1015 Lausanne Switzerland

[4]Institut Photovoltaïque d'Île-de-France (IPVF), 18 Boulevard Thomas Gobert, Palaiseau, 91120, France

[5]Électricité de France (EDF), R&D, 18 Boulevard Thomas Gobert, Palaiseau, 91120, France

[6]CNRS UMR 9006, 18 Boulevard Thomas Gobert, Palaiseau, 91120, France

[7]Laboratoire de Réactivité et Chimie des Solides, CNRS UMR7314, Université de Picardie Jules Verne, Hub de l'énergie, 15 rue Baudelocque, 80039 Amiens, France

# The authors contributed equally

*Aldo.dicarlo@uniroma2.it

Abstract

High band gap semi-transparent solar cells based on $CH_3NH_3PbBr_3$ perovskite are attractive for building integration, tandem cells and electrochemical applications. The lack of control of the

$CH_3NH_3PbBr_3$ perovskite growth limit the exploitation of $CH_3NH_3PbBr_3$-based perovskite solar cells. In this paper, we introduce a post-treatment performed after the initial $CH_3NH_3PbBr_3$ crystallization based on methylamine gas that drastically enhances the perovskite quality leading to a highly cristalline film with improved average visible transmittance (AVT) close to 56%. Opaque devices showed outstanding results in terms of open-circuit voltage and power conversion efficiency (PCE) reaching 1.54 V and 9.2%, respectively. These achievements are ascribed to a film with reduced morphological defects and better interface quality and reduced non-radiative pathways. For the first time, the fabrication of semi-transparent $CH_3NH_3PbBr_3$-based solar cells is demonstrated reaching a maximum PCE equal to 7.6%, an AVT of the full stack device of 52% and an excellent light stability at maximum-power point tracking.

1. Introduction

Organic-inorganic hybrid perovskites are promising materials for thin-film solar cell technology due to their high power-conversion efficiencies and solution process ability[1]. The best performing perovskite materials so far are relying on iodide-based compositions (such like $CH_3NH_3PbI_3$ and $HC(NH_2)_2PbI_3$) or mixed iodide/bromide solid solutions leading to an optical bandgap in the range of 1.5-1.6 eV, not far from the theoretical optimum bandgap value that range between 1.2-1.4 eV for ideal solar cells[2]. Pure bromide-based compositions entail a wider optical bandgap transition and hence penalise the achievement of high power conversion efficiency (PCE)[3, 4]. Nevertheless, the development of these bromide systems are very attractive due to the improved visible transparency and the higher open-circuit voltage values[5] that make them a potential candidate for electrochemical applications[6], building integration photovoltaics (BIPV)[7] and all-perovskite tandem solar cells[8]. Furthermore, their high photoluminescence quantum efficiencies attract huge interest for their integration as new emitters for light-emitting diodes (LEDs)[9, 10].

There have been several efforts to develop the $CH_3NH_3PbBr_3$–based solar cells technology[5, 11] leading so far to a record PCE of 10.4% on opaque devices[4]. One crucial issue to address in these systems is the large internal energy losses that manifest in the large difference (exceeding 0.6 V) between the optical bandgap and the open-circuit voltage measured under illumination [12]. This voltage loss is mainly ascribed to both the non-radiative recombination due to intra-bandgap states and misalignment of the energy levels between the absorber and the selective transport layers [13]. Non-radiative energy losses can be mitigated by grain boundary and punctual surface defects passivation using molecular Lewis base additives [14, 15], cross-linking agents [16] and defect-healing induced by using methylamine (MA) gas [17].

In 2015, Zhou et al. [17] proposed a method for microstructural defect healing of $MAPbI_3$ perovskite films by using methylamine gas. They reported the healing process based on formation of a transparent of $CH_3NH_3PbI_3 \cdot xMA$ intermediate having liquid state, which ultimately results into a smoother and higher crystallinity film after methylamine exposure. MA treatment has been then applied to $CH_3NH_3PbI_3$ [18, 19, 20], $CH_3NH_3PbI_2Br$[19], $CsPbBr_3$[21] and $Cs_xMA_{1-x}PbI_{3-x}Br_x$[22]. The application to $CH_3NH_3PbBr_3$ system has been reported from Zhang et al. in 2016 [23]. The authors reported the use of MA in association with $PbBr_2$ to create a highly luminescent $CH_3NH_3PbBr_3$ perovskite planar film. Chih et al. used MA treatment of $CH_3NH_3PbBr_3$ films through a solid reaction between MACl and KOH powders at room temperature in order to fabricate a planar perovskite-based LEDs[9]. In this work, we report an easy, fast and efficient procedure through the exposition of the $CH_3NH_3PbBr_3$ film to methylamine gas that significantly improve the film's characteristics and the photovoltaic performance of device based on mesoporous TiO_2 (mp-TiO_2) scaffold. The MA treatment triggers the defect healing of the initial rough and haze perovskite film leading to a transparent and smooth film with passivated grain-boundaries. Interestingly, this methodology is versatile regardless of the deposition procedure (ie. solvent quenching or double-step) and the environment (N_2 or in air) selected for the initial film's crystallization. Moreover, the MA

treated films show improved visible transparency, higher photoluminescence, higher crystallinity, passivated grains, and hence enabling better charge transport and high efficiency $CH_3NH_3PbBr_3$ solar cells.

2. Results and discussion

Figure 1 gives a schematic representation of the thin film preparation process for $CH_3NH_3PbBr_3$ prepared by spin-coating technique. It consists of two processing steps. The first step is performed using the solvent quenching method by spin-coating deposition of a stoichiometric solution of CH_3NH_3Br and $PbBr_2$ in DMSO solvent and using toluene as an anti-solvent. The resulting orange film shows a rough and hazy surface after the rapid conversion of the film into crystalline $CH_3NH_3PbBr_3$ when annealing at 80 °C. The second step, here after called MA treatment, is performed by the exposure of the film to MA vapour for few seconds. This exposure leads to an instantaneous conversion of the original $CH_3NH_3PbBr_3$ into a fully transparent and colourless intermediate liquid phase $CH_3NH_3PbBr_3 \cdot xCH_3NH_2$ in analogy with what has been proposed by Zhou et al.[17] and Raga et al.[20] in the case of $CH_3NH_3PbI_3$:

$$CH_3NH_3PbBr_3\ (s) + MA(g) \rightarrow CH_3NH_3PbBr_3 \cdot xCH_3NH_2(l)$$

The gas-perovskite interaction behaviour is fully investigated by Zhou and here extended to the $CH_3NH_3PbBr_3$ perovskite. In particular, the CH_3NH_2 molecules react with the inorganic PbI_6^- octahedra framework of the perovskite resulting in the complete collapse of that structure into a liquid.

Upon removal of the film from the MA gas exposure, it converts instantaneously (less than one second) into a smooth, more yellowish and more transparent film. In fact, the degassing of the CH_3NH_2 molecules leads to the reconstruction of the $CH_3NH_3PbBr_3$ perovskite. A movie depicting the whole MA treatment and effect on the film is reported in supplementary section.

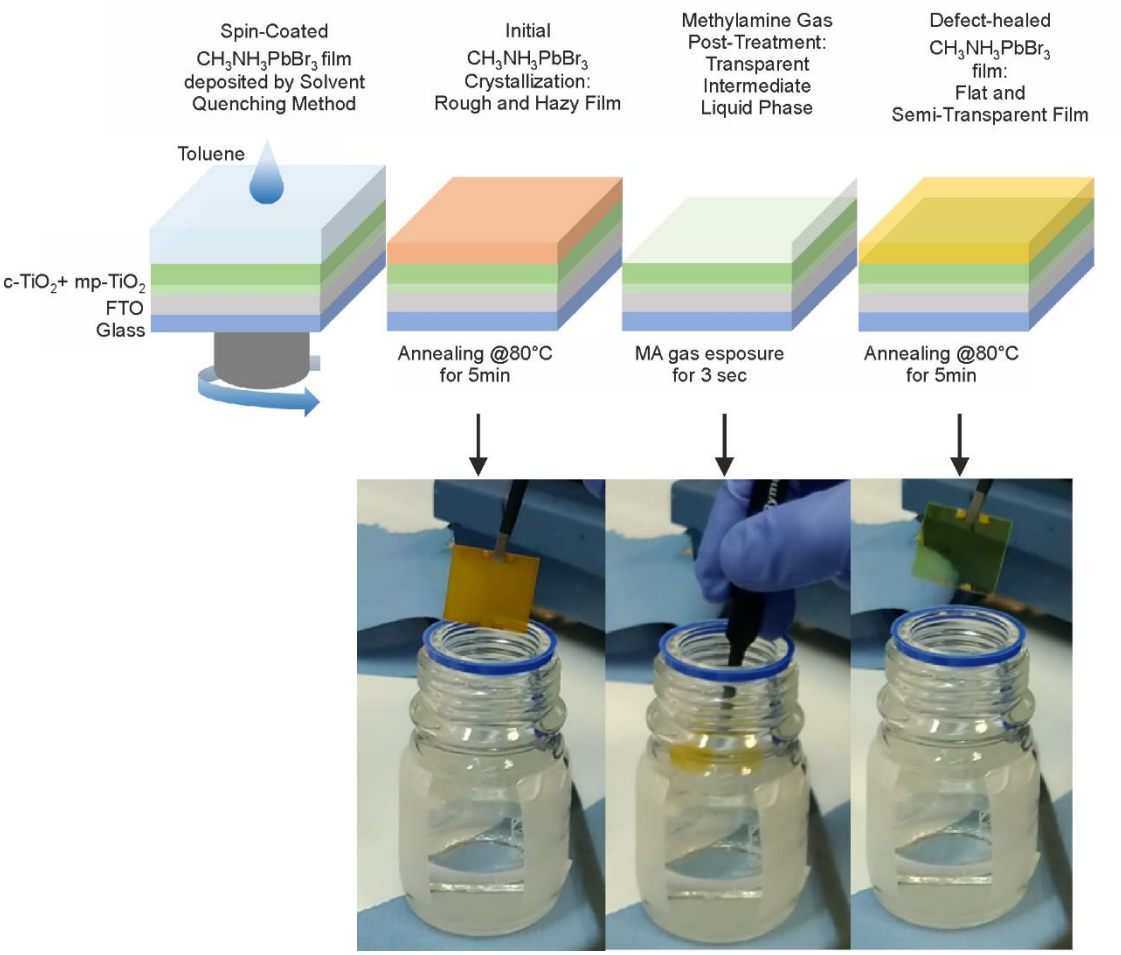

Figure 1. Schematic of the two-step crystallization process with intermediate MA gas treatment (Initial Crystallization and MA Gas Post-Treatment) of the $CH_3NH_3PbBr_3$ film deposited on Glass/FTO/c-TiO_2/mp-TiO_2 substrate.

The images of the $CH_3NH_3PbBr_3$ films deposited on FTO/c-TiO_2/mp-TiO_2 substrates before (called control) and after the MA treatment (called MA-treated) are reported in Figure 2a to highlight the improvement in visible transparency thank to the proposed post-treatment. Transmittance/Reflectance spectra of the obtained films are reported in Figure 2b for control and MA-treated samples. The results show a very clear enhancement in the optical properties of the MA-treated film which translates into a reduction of the reflectance in the whole visible and NIR range and a noticeable improvement by ~20 % of the film transmittance reaching a maximum of 80 % for wavelengths above the absorption tail. This improvement is attributed to

the reduction of the film's haze induced by the multiple light interactions with the morphological defects present in the non-treated film (pinholes and surface roughness). As a result, the Average Visible Transmittance (AVT) metric[7] is remarkably increased from 39.5 % to 56.0 %, a value becoming of higher interest for semi-transparent BIPV applications.

Considering that $CH_3NH_3PbBr_3$ has a direct allowed bandgap transition[24], the Tauc plot comparison reported in Figure 2c confirm a slight but visible widening of the perovskite's bandgap energy from 2.31 eV to 2.34 eV subsequently to the MA treatment, corresponding to a blue-shift of 7 nm absorption edge (Figure S1). This blue shift of the absorption edge for MA-treated film explains the eye perception of a colour transition from orange to yellow after the gas treatment (Figure 2a). The ln(α) vs. photon energy plot (Figure 2d) provides important insight into the impact of the MA-treatment in the level of sub-bandgap states resulting from the density of surface defects. In fact, the MA treatment affords a decrease in the Urbach tail energy from 36 meV to 25 meV.[25]

Steady-state photoluminescence (PL) spectra of $CH_3NH_3PbBr_3$ films deposited on glass and in the complete glass/ FTO/c-TiO_2/mp-TiO_2/Perovskite/PTAA stack are reported in Figure 2c and 2d, respectively. The MA-treated film deposited on glass shows a higher PL intensity and narrower emission linewidth compared to the control sample by ca. 10 nm. This suggests that the MA exposure contributes to reduce the non-radiative deactivation pathways as a consequence of the reduction of intra-bandgap states (Figure 2d). The PL maximum is also blue shifted by 7 nm in good agreement with the bandgap widening. For the complete stack, the MA-treated film shows a PL quenching higher than control device due to non-radiative quenching of the carriers at the interface with the selective transport layer. [15, 20] Regardless of MA treatment, it is worth mentioning that we reproducibly experienced an important enhancement of the PL intensity of $CH_3NH_3PbBr_3$ films when this is in contact with TiO_2 layers (Figure S2). This enhancement of PL intensity, without any noticeable change in the emission band position and shape, is more pronounced for a non-MA treated film (+850 %) compared to a treated MA

film (+450 %). This result gives a strong indication that the perovskite layer when infiltrated into the mesoporous layer of TiO_2 is less defective than the same film deposited on glass.

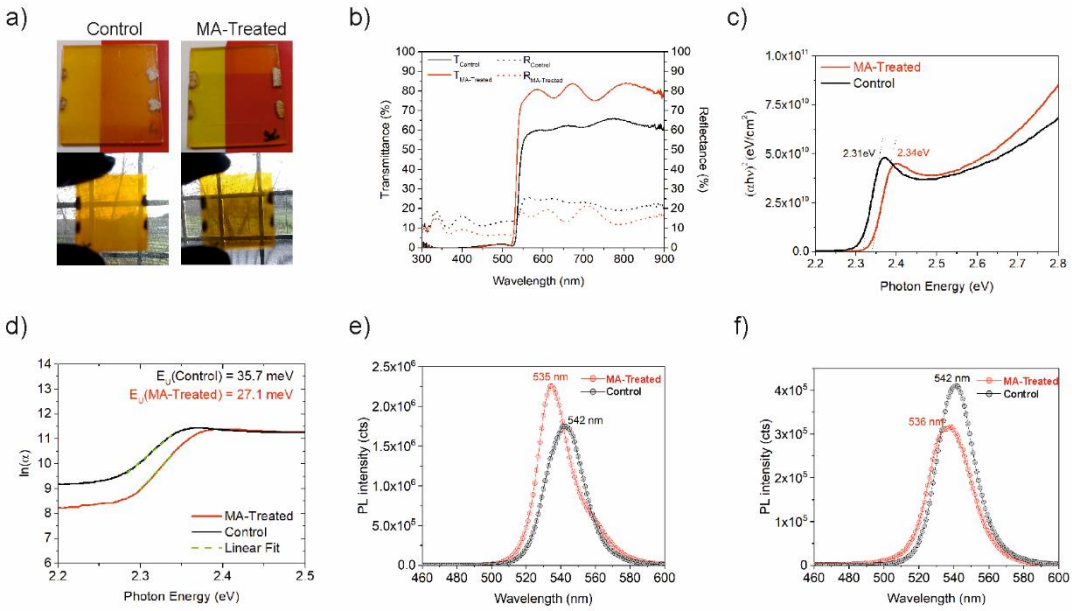

Figure 2. a) Images of control and MA-treated perovskite layers. b) Transmittance (solid curves) and reflectance (dashed curves) spectra of Glass/FTO/c-TiO_2/mp-TiO_2/$CH_3NH_3PbBr_3$ stack for control (black curve) and MA-treated (red curves) devices. c) Tauc plot calculated for an absorber thickness of 500 nm. d) Natural logarithm of the absorption coefficients (α) vs. photon energy plots. The Urbach energies are calculated from the inverse of the slope of the linear fitting (green dotted lines) for Control (black curves) and MA-Treated Devices (red curves). Comparison of Steady-State Photoluminescence spectrum of Glass/ $CH_3NH_3PbBr_3$ (e) and Glass/FTO/c-TiO_2/mp-TiO_2/ $CH_3NH_3PbBr_3$/PTAA (f) for control (black curves) and MA-treated (red curves) samples (excitation at 450 nm, excitation and emission slit bandwidth of 1 nm).

To grasp further insights on the structural difference between the perovskite film obtained with MA treatment, X-ray diffraction analysis has been carried out (Figure 3a-b). $CH_3NH_3PbBr_3$

crystallizes in a cubic lattice within Pm-3m space group. Both films are highly textured with strong preferential orientation along (00l) planes. The lattice cell parameter refined in full pattern matching mode for the control film is a = 5.9309(2) Å and a = 5.9305(2) Å for the MA-treated film. This result endorses the conclusion that the film stoichiometry and bulk point defects are not modified by the recrystallization induced by the MA treatment. However, we systematically noticed higher intensities of the diffraction peaks in the case of the MA-treated films which indicate that the latter become even more textured after the recrystallization. A difference in film's texturing has been also reported by Zhou et al. in the case of $CH_3NH_3PbI_3$ thin films (tetragonal crystal structure, S.G. I4/mcm) for which a MA-treatment favours the recrystallization of the (110) plane, corresponding to the denser Pb^{2+} / I^- plane in $CH_3NH_3PbI_3$[17].

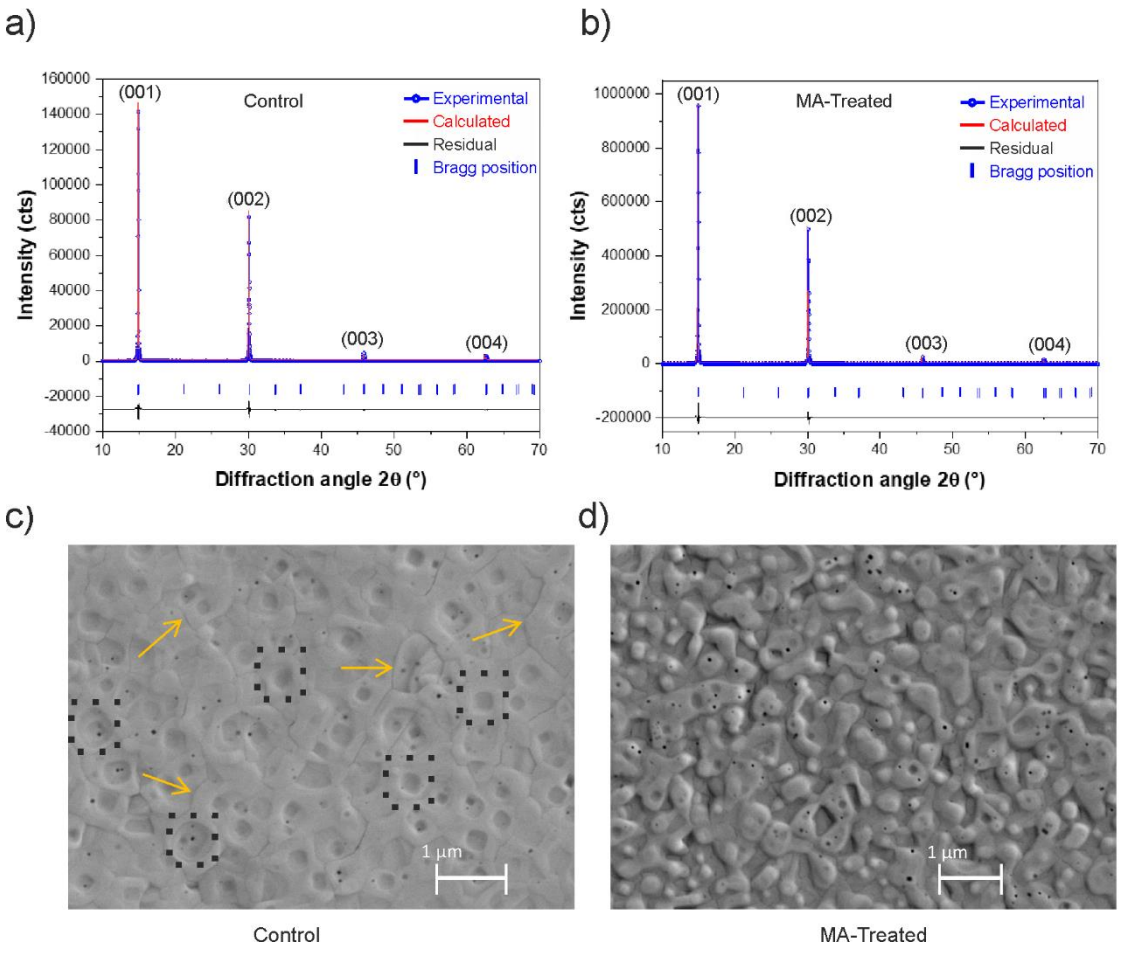

Figure 3. X-ray diffraction patterns refined of control (a) and methylamine-treated (b) perovskite films. c-d) Top view SEM images of the control (c) and methylamine-treated (d) perovskite films deposited upon glass FTO/compact-TiO_2/meso-TiO_2 substrate. The arrows in figure (c) indicate the presence of cracks at the grain boundaries of the control film. Dotted squares in figure (c) represent the defects in the perovskite film.

The top-view SEM pictures at the same magnification reveal noticeable modifications on the film's morphology after recrystallization. In control sample, the film shows the formation of large crystallites (highlighted in Figure 3c with dotted squares) and cracks at the grain boundaries (as indicated from yellow arrows in Figure 3c). By contrast, the MA-treated sample shows a coalescence phenomenon between crystals after the treatment which is driven by the very fast process of dissolution / recrystallization induced by the exposure of MA vapour and its release in ambient conditions. The films are becoming crack-free as a result of the defect healing process induced by methylamine gas exposure.[17] The impact of the MA treatment on full devices is evaluated by the fabrication of opaque cells with FTO/c-TiO_2/mp-TiO_2/$CH_3NH_3PbBr_3$/PTAA/Au architecture.

The statistical results collected on a batch of 26 different cells show unambiguously a remarkable increase of all the photovoltaic parameters thanks to the fast and easy MA treatment (Figure S3a-c). The main affected metric is the short-circuit photocurrent density which is enhanced by between 2 to 3 mA/cm^2. As a result, the average PCE value is boosted to 7.3 % under A.M.1.5G conditions compared to 4.4% for control devices. Figure 4b reports the (J-V) curves measured under reverse and forward scan for the champion devices based either on a control $CH_3NH_3PbBr_3$ layer or same with MA treatment. The MA treatment improves the champion device performance from a PCE of 5.1 % (J_{sc} = 5.4 mA/cm^2, V_{oc} = 1.37 V, FF = 68.9%) to 9.1% (J_{sc} = 8.0 mA/cm^2, V_{oc} = 1.52 V, FF = 73.6 %). Such a high PCE is very well-

maintained under maximum power point conditions (Figure S3d). In both cases, a negligible *J-V* hysteresis between reverse and forward scan is observed.

These results are well corroborated by the External Quantum Efficiency (EQE) spectra reported in Figure 4c. For the MA-treated $CH_3NH_3PbBr_3$ film, the EQE reaches a plateau between 380 and 530 nm with a maximum EQE of ca. 90 %. Considering light losses by reflections on glass, these results suggest that the MA-treated film produces a photo-current which is very close to the theoretical limit. The J_{SC} obtained by integrating the EQE with the 1 Sun A.M. 1.5G spectrum, shows a perfect match with respect to the one measured directly under the sun simulator for the MA-treated PSC, whereas a minor difference (~ 0.5 mA/cm^2) is obtained for the control device. This feat is a direct consequence of the film quality improvement obtained after recrystallization which affords enhanced extraction of carriers as deduced by TCSPC experiments and their collection which should be close to 100 % efficiency in this case. Figures S5 and 4d show the PL decay comparison of $CH_3NH_3PbBr_3$ without and with MA induced recrystallization on glass or the same layer in contact with TiO_2. On glass, two contributions are required to account for the total decay. Two contributions are most of time encountered in perovskites. The laser fluence herein used of 5 $nJ.cm^{-2}$ generates a carrier density of ca. $1.5.10^{15}$ cm^{-3} in the film, which affords to avoid Auger processes in the recombination rate. The fast contribution given the low excitation laser power is attributed to the initial filling of the traps by the photo-generated carriers as recently highlighted by Herz et al. [26] (Figure S4). Few nanoseconds after the excitation pulse, the PL transient shows a dominant monoexponential decay corresponding to the band-to-band recombination dynamics (bimolecular recombination). The halftime value is in the range of 50 ns for both films. This result suggests that the MA-treatment does not modify bimolecular recombination dynamics, thus has no noticeable influence on the level of bulk point defects in agreement with the XRD results showing unchanged lattice cell parameters. The same film in a full device illuminated from

TiO_2 side shows a faster decay owing to carrier diffusion towards the selective contacts, filling the traps by photo-induced carriers and their extraction [27]. The light penetration is estimated to be 170 nm at 475 nm considering the absorption coefficient $\alpha_{475nm} = 5.8.10^4$ cm^{-1}, thus only TiO_2 / perovskite interface and the core of the perovskite film is probed. After MA-treatment, the PL dynamic is accelerated nearly two times indicating a more favourable electron extraction after this treatment in agreement with the improved perovskite infiltration and the higher EQE after recrystallization.

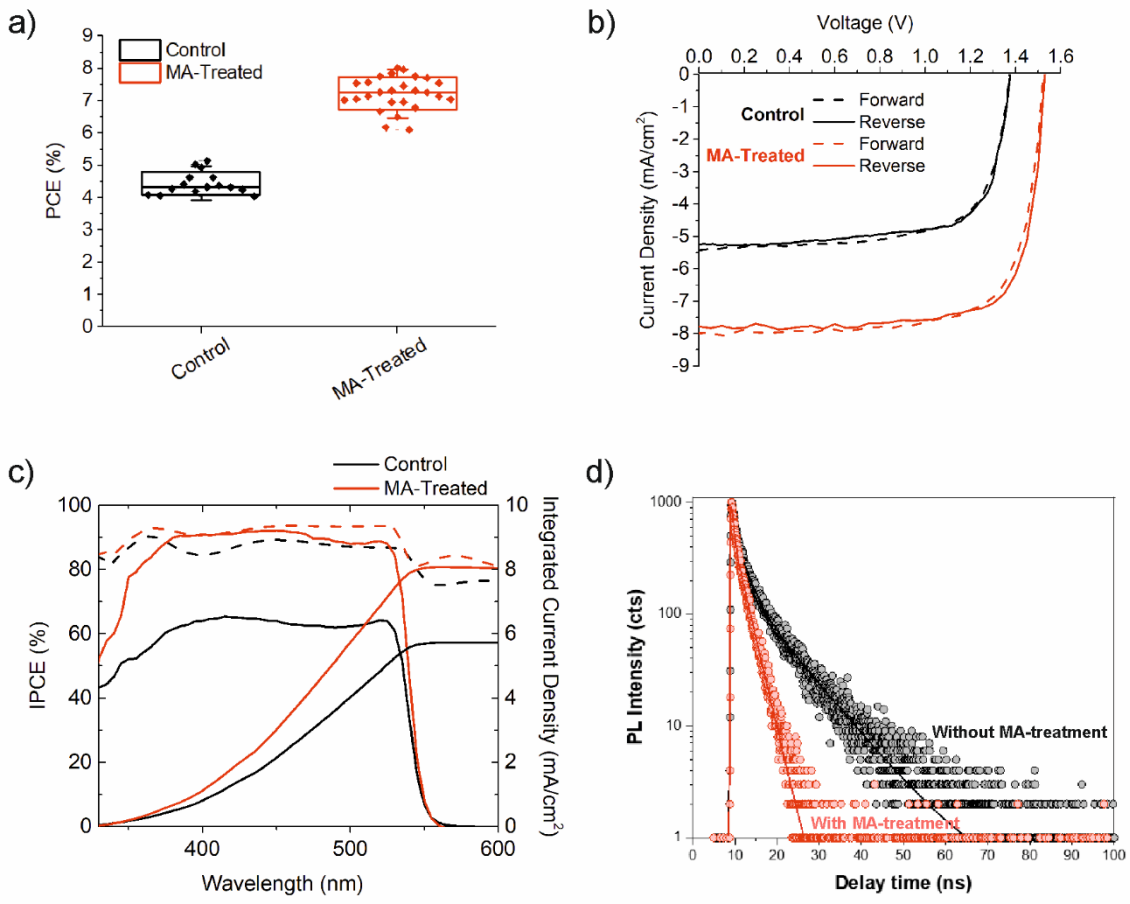

Figure 4. a) Box chart of the PCE values measured for a batch of 26 devices made of control and MA-treated $CH_3NH_3PbBr_3$. b) J-V curves of the champion control and MA-treated PSC cells measured under 1Sun A.M.1.5G illumination conditions in forward (dashed curves) and reverse (solid curves) scan direction. c) Incident Photon-to-Current Efficiency (EQE), 100-R in dashed curves and integrated current density for control and MA-treated devices. d) Time-

Correlated Single Photon Counting experiment on FTO/compact-TiO_2/meso-TiO_2/perovskite/PTAA device with and without methylamine treatment. The PL decay is recorded at 475 nm excitation (5 $nJ.cm^{-2}$ pulse energy) and probing the emission at 540 nm with 10 nm bandwidth. The illumination is carried out from TiO_2 side to probe TiO_2/perovskite interface.

In addition to the higher photo-current, a higher photo-voltage is also obtained for the films treated with MA (Figure S3a). This enhancement of ca. 175 mV in average is the result from the greater contact between TiO_2 and the perovskite and the reduced Urbach-tail energy.

We should point out that the MA treatment, triggering an extremely fast solid-to-liquid transition upon exposure and liquid-to-solid transition during withdraw, improves the pore filling resulting a better infiltration of the perovskite into the mp-TiO_2 which favours the charge extraction as supported by TCSPC and assist the enhancement of charge collection efficiency of the device towards 100 %. The role of pore filling on the charge collection is further investigated by performing optical[28] and drift-diffusion (DD) simulations[29] on different structures with the aim to reproduce the experimental performance of the MA-treated and control devices.

Assuming that the MA gas treatment allows to have a perfect pore-filling fraction (PFF) of the mesoporous scaffold (PFF=100%), we varied PFF from 100% down to 53%, considering a mp-TiO_2 volume porosity to 50%[30] as shown in Figure S5. The choice of the device thickness for the MA-treated device is made according to the experiments, such that the active region is composed by a 150nm-thick mp-TiO_2:$CH_3NH_3PbBr_3$ and a 280nm-thick $CH_3NH_3PbBr_3$ overlayer. Figure 5a shows the comparison between the structure modelling and cross-section SEM images for the control and MA-treated devices. Low magnification cross-section SEM images are also reported in Supporting Information as Figure S6.

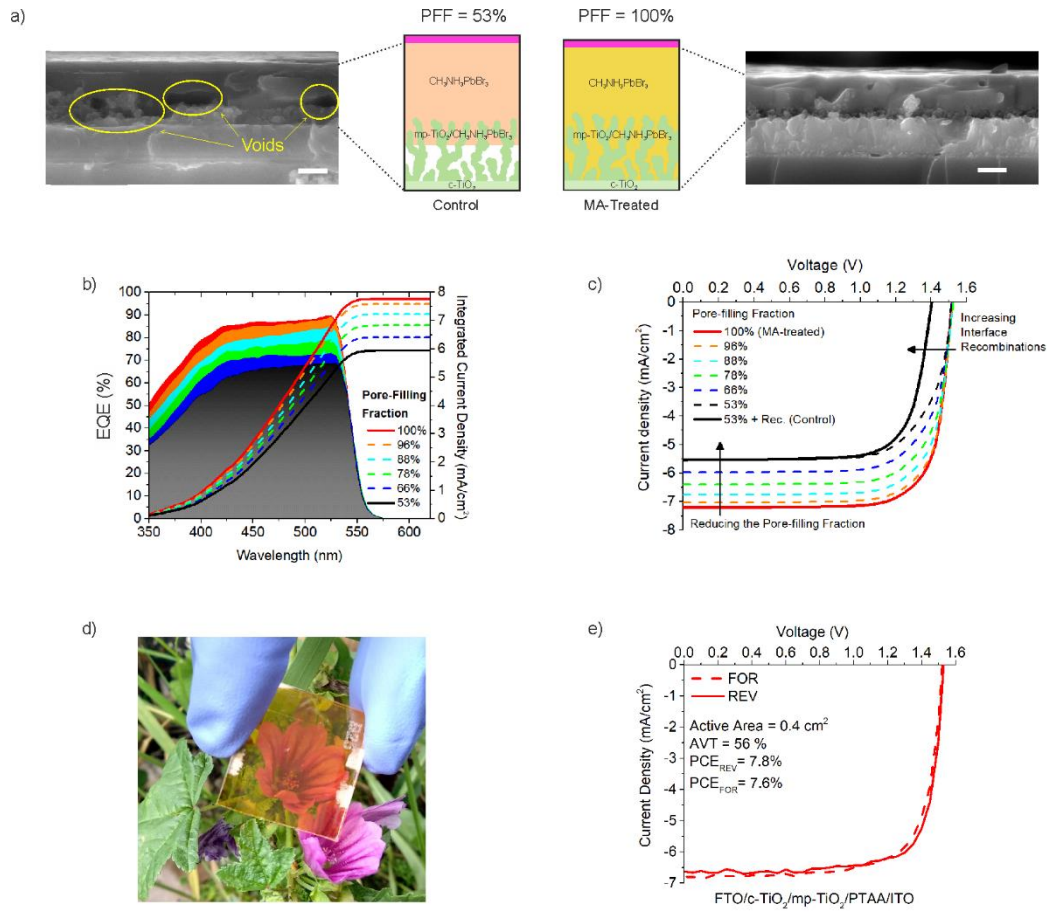

Figure 5. a) Control (PFF=53%) and MA-treated (PFF=100%) device structure for FTO/c-TiO_2(30nm)/mp-TiO_2(150nm)/$CH_3NH_3PbBr_3$(t_{PSK})/PTAA(25nm)/Gold used in drift-diffusion simulations and corresponding cross-sectional SEM images. The scale bar is equal to 200nm for both images. Notably, the thickness of the $CH_3NH_3PbBr_3$ overlayer is ruled by the following: t_{PSK} = 280nm – P/100 · (1-PFF/100) · $t_{mp\text{-}TiO2}$. b) Theoretical EQE and integrated current density obtained with optical calculations by varying the PFF from 100% to 53%. c) Comparison of theoretical J-V curves for the control (black), MA-treated (red), and intermediate structures (dashed lines) obtained by DD simulations for different pore-filling fraction values. d) Picture of the semi-transparent cell made on FTO/c-TiO_2/mp-TiO_2/$CH_3NH_3PbBr_3$/PTAA/ITO stack. e) J-V curves of the champion semi-transparent PSC

cells measured under 1 sun A.M.1.5G illumination conditions in forward (dashed curve) and reverse (solid curve) scan directions.

Optical calculations pointed out that the presence of voids leads decreases the quantity of the absorbed light within the active region (see Figure S7). This primary worsening of performance becomes apparent from the drift-diffusion simulation results shown in Figure 5d. Indeed, the further decrease of J_{sc} (e.g. in the control device from 5.94 to 5.55 mA/cm^2) accompanied by a lower fill-factor is attributable to the minor charge collection. This is basically due to the reduced contact surface between the mp-TiO_2 and $CH_3NH_3PbBr_3$. Whereas, the open-circuit voltage (V_{oc}) drop of around 110 mV from MA-treated to control (from 1.52 to 1.4 V) is attributable to the interface recombination. Indeed, on the basis of the measured lifetimes by transient PL decay, we assumed a stronger interface recombination for the control device at mp-TiO_2/$CH_3NH_3PbBr_3$.

The benefit of the methylamine treatment is also demonstrated using a double-step deposition method for the same $CH_3NH_3PbBr_3$ device stack made entirely in air. In Figure S8, the *J-V* curves and the MPPT measurement for control and MA-treated samples using this methodology are reported. The results show an improved PCE, going from 5.5% to 8.2% after the MA-treatment thanks again to a noticeable enhancement in both J_{sc} and V_{oc} values. This highlights that the MA-treatment is a universal defect-healing method to improve the performances and semi-transparency of PSCs based on $CH_3NH_3PbBr_3$ perovskite, regardless of the environment and the deposition method for processing the perovskite film.

The main advantage of increasing the optical bandgap of the perovskite to a value of ca. 2.3 eV is for semi-transparent applications such as for BIPV and non-intrusive PV. For the first time, optically opaque gold back-contact has been replaced by optically transparent RF-sputtered ITO electrode in $CH_3NH_3PbBr_3$-based devices. Our previous work demonstrated the effectiveness of the sputtered ITO electrode on top of the PTAA polymer without using buffer layers[31]. The

transparent 110nm-thick ITO electrode has been optimized to reach a very high AVT of 85 % without penalizing the sheet resistance value measured to be 34 Ω/□. The average results obtained on a batch of twenty MA-treated semi-transparent devices show an AVT and PCE of 52% and 6.75%, respectively on active area of 0.4 cm^2 (Figure S9). This leads to a light utilization efficiency (LUE) of 3.5 % [7]. A picture of the semi-transparent MA-treated device is reported in Figure 5d in order to appreciate the visible transparency of the full stack. The champion cell showed PCE values equal to 7.8% and 7.6% when measured respectively under reverse and forward scan directions demonstrating negligible hysteresis. In order to test the shelf life of semi-transparent MA-treated, the device is stored for 160 days in air under dark condition (Figure S10a). No degradation is shown demonstrating impressive environmental stability of the MA-treated and ITO-based devices. Furthermore, the light soaking test at MPP was performed by following the ISOS-L-1 protocol reported from Khenkin et al.[32] (Figure S10b). As a result, the non-encapsulated device is stable after 270 hours under operative working conditions considering the initial PCE value, thus demonstrating that MA-treatment permits the fabrication of highly efficient, transparent and stable $CH_3NH_3PbBr_3$-based devices.

3. Conclusion

In conclusion, we fabricated $CH_3NH_3PbBr_3$ perovskite solar cell with a PCE exceeding 9% and 7.5% for opaque and semi-transparent cells, respectively showing negligible *J-V* hysteresis and excellent fill factor. For semi-transparent cells, full device stack showed high AVT value equal to 52% without means of anti-reflective coating and a high operative stability at MPP condition in air. This has been achieved by employing a rapid and easy treatment of the deposited perovskite film by MA gas. This MA-treatment affords to reach an open-circuit voltage higher than 1.5 V, thus minimizing internal energy losses. The XRD, SEM, TCSPC and steady-state PL measurements endorse the morphological improvement and the obtain of a less defective perovskite film after such MA exposure. This leads to a remarkable enhancement of the photo-current produced by the film. This work underlines that the MA treatment is a versatile defect

healing method to fabricate highly efficient, transparent and stable PSC based on $CH_3NH_3PbBr_3$ composition.

4. Material and Methods

4.1. **Materials:** Titanium diisopropoxide bis(acetylacetonate), Methylamine in Ethanol solution, TBP and all the solvents used are purchased from Sigma-Aldrich. 30NR-D TiO_2 colloidal paste and CH_3NH_3Br are purchased from Greatcell Materials. $PbBr_2$ is purchased from TCI. PTAA polymer (10kDa) is purchased from Solaris Chem. ITO cathode (90-10 wt% target, 99.99%) is purchased from Testbourne Ltd.

4.2. **Device Fabrication:** Fluorine-doped Tin Oxide (FTO) glass substrate (Pilkington) are etched by using pulsed UV laser in order to obtain the required etching lines for insulation of four pixels-based devices. The etched FTO glass substrates are cleaned by ultrasonic batch in acetone and 2-propanol for 10minutes for each solvent. Furthermore, a 30nm-thick compact TiO_2 layer is deposited on clean FTO substrate, using spray-pyrolysis. Then, a 220nm thick mesoporous TiO_2 is spin coated on the compact TiO_2 layer. After that, the samples are kept under UV lamp for 10minute to increase TiO_2 surface wettability [57][58]. Then, the perovskite films are deposited by spin coating at 4000rpm for 20s using a 1.4M $CH_3NH_3PbBr_3$ solution in DMSO obtained by mixing CH_3NH_3Br and $PbBr_2$ precursors. The solvent-quenching method using toluene as anti-solvent is performed 10s before the end of the spin coating program. After spin coating, the samples are kept on a hot plate at 80°C for 3-4 minutes. In the second step, the annealed $CH_3NH_3PbBr_3$ films are exposed to Methylamine gas for 1-2 seconds. The procedure is reported in the supporting video showing the entire MA-treatment performed in air and fully explained in Figure 1. After the MA treatment,

the sample are again annealed at 80°C to remove any by-product of the reaction. Furthermore, doped (10µl/ml TBP and 5ul/ml of 180mg/ml LiTFSI solution in ACN) PTAA is deposited on the perovskite film using spin coating (4000 rpm for 20 sec). After the PTAA deposition, thermally evaporated gold electrodes are deposited at evaporation rate of 0.3A/s for the first 10nm and then increased to 1A/s for the rest of the process resulting in a thickness of 80nm. For semi-transparent devices, 110nm-thick low ITO electrodes made by RF sputtering at low power density (0.26 W/cm^2) and at low temperature are performed.

4.3. **Characterization techniques:** X-ray diffraction study was made using a Bruker D8 Cu Kα diffractometer in θ-2θ Bragg-Brentano configuration. Steady-state fluorescence and Time-Correlated Single Photon Counting (TCSPC) experiments were carried out on Edinburgh Instrument FLS980 spectrometer equipped with a 450 W Xe arc lamp for steady-state measurements with two excitation/emission monochromators (excitation/emission bandwidth of 2 nm). TCPSC were acquired in front phase configuration using a 475 nm pulsed laser diode (FWHM 70 ps) at 1MHz. A MCP-PMT detector (Hamamatsu) is set after the first emission monochromator. A long-pass filter at 495 nm was used to avoid direct light scattering contributions to be detected. The typical IRF value in this configuration is in the range of 100 ps. For TCSPC, the slit bandwidth of the monochromator was set at 10 nm to maximize the PL intensity from the samples. The excitation energy from the laser diodes is ca. 5 nJ/cm^2. Transmittance and Reflectance spectra were carried out by using an UV−vis spectrophotometer equipped (Shimadzu UV-2550) with an integrating sphere. J−V characteristics were measured with a class A sun simulator (ABET) under AM 1.5G 1 sun illumination condition. The AM1.5G condition is obtained by using an optical filter. The sun simulator was calibrated using a Si reference cell (RR-226-O, RERA Solutions). An active area of 0.17cm^2 for opaque cells (0.4cm^2 for semi-transparent

ones) was determined by a metal mask. The J-V curves were scanned with the rate of 300 mV s-1 without any preconditioning. The J-V curves are firstly measured under forward scan (from Jsc to Voc) and then reverse scan (from Voc to Jsc). The MPPT protocol is made by polarizing the device at MPP after JV scans and it applied a small perturbation of both VMPP and JMPP to obtain the dynamic MPP Tracking. EQE analysis was performed with a commercial apparatus based on a 300 Watts Xenon lamp monochromatic light (300–1100 nm @ 2 nm of resolution) with thermal controlled stage. J-V, MPPT and EQE measurements were performed by using a commercial apparatus (Arkeo – Cicci Research s.r.l). SEM images were acquired by using a Zeiss Merlin VP compact microscope. The field emitting gun was operated at an acceleration voltage of 5keV. Images were obtained in secondary electron detection mode.

Acknowledgments

The authors acknowledge “IMPRESSIVE” project which received funding from the European Union’s Horizon2020 research and innovation program under grant agreement number N° 826013. S.C. would like to thank funding from the European Union’s Horizon 2020 research and innovation program under the Marie Skłodowoska-Curie Grant Agreement N 845612. A.S. and A.G. acknowledge funding by the International Graduate School of Science and Engineering (IGSSE), TUM. A.S. thanks German Academic Exchange Service (DAAD) for funding 91650212 via funding program 57299294.

References

[1] A. Kojima, K. Teshima, Y. Shirai, T. Miyasaka, Journal of the American Chemical Society 2009, 131, 6050; J.-P. Correa-Baena, M. Saliba, T. Buonassisi, M. Grätzel, A. Abate, W. Tress, A. Hagfeldt, Science 2017, 358, 739; S. D. Stranks, G. E. Eperon, G. Grancini, C. Menelaou, M. J. P. Alcocer, T. Leijtens, L. M. Herz, A. Petrozza, H. J. Snaith, Science 2013, 342, 341; H.-S. Kim, C.-R. Lee, J.-H. Im, K.-B. Lee, T. Moehl, A. Marchioro, S.-J. Moon, R. Humphry-Baker, J.-H. Yum, J. E. Moser, M. Grätzel, N.-G. Park, Scientific Reports 2012, 2, 591; M. M. Lee, J. Teuscher, T. Miyasaka, T. N. Murakami, H. J. Snaith, Science 2012, 338, 643; M. A. Green, A. Ho-Baillie, H. J. Snaith, Nature Photonics 2014, 8, 506.

[2] W. Shockley, H. J. Queisser, Journal of Applied Physics 1961, 32, 510; W. Tress, Advanced Energy Materials 2017, 7, 1602358; W. E. I. Sha, X. Ren, L. Chen, W. C. H. Choy, Applied Physics Letters 2015, 106, 221104.
[3] R. Comin, G. Walters, E. S. Thibau, O. Voznyy, Z.-H. Lu, E. H. Sargent, Journal of Materials Chemistry C 2015, 3, 8839; Z. Song, C. Chen, C. Li, R. A. Awni, D. Zhao, Y. Yan, Semiconductor Science and Technology 2019, 34, 093001.
[4] J. H. Heo, D. H. Song, S. H. Im, Advanced Materials 2014, 26, 8179.
[5] Y. Liang, Y. Wang, C. Mu, S. Wang, X. Wang, D. Xu, L. Sun, Advanced Energy Materials 2018, 8, 1701159; W. S. Subhani, K. Wang, M. Du, X. Wang, N. Yuan, J. Ding, S. Liu, Journal of Energy Chemistry 2019, 34, 12; S. Ryu, J. H. Noh, N. J. Jeon, Y. Chan Kim, W. S. Yang, J. Seo, S. I. Seok, Energy & Environmental Science 2014, 7, 2614; X. Hu, X.-F. Jiang, X. Xing, L. Nian, X. Liu, R. Huang, K. Wang, H.-L. Yip, G. Zhou, Solar RRL 2018, 2, 1800083.
[6] Q. Wang, L. Tao, X. Jiang, M. Wang, Y. Shen, Applied Surface Science 2019, 465, 607.
[7] C. J. Traverse, R. Pandey, M. C. Barr, R. R. Lunt, Nature Energy 2017, 2, 849.
[8] J. H. Heo, S. H. Im, Advanced Materials 2016, 28, 5121; R. Sheng, A. W. Y. Ho-Baillie, S. Huang, M. Keevers, X. Hao, L. Jiang, Y.-B. Cheng, M. A. Green, The Journal of Physical Chemistry Letters 2015, 6, 3931; R. Sheng, M. T. Hörantner, Z. Wang, Y. Jiang, W. Zhang, A. Agosti, S. Huang, X. Hao, A. Ho-Baillie, M. Green, H. J. Snaith, The Journal of Physical Chemistry C 2017, 121, 27256; A. Singh, A. Gagliardi, Solar Energy 2019, 187, 39.
[9] Y.-K. Chih, J.-C. Wang, R.-T. Yang, C.-C. Liu, Y.-C. Chang, Y.-S. Fu, W.-C. Lai, P. Chen, T.-C. Wen, Y.-C. Huang, C.-S. Tsao, T.-F. Guo, Advanced Materials 2016, 28, 8687.
[10] Y. Cao, N. Wang, H. Tian, J. Guo, Y. Wei, H. Chen, Y. Miao, W. Zou, K. Pan, Y. He, H. Cao, Y. Ke, M. Xu, Y. Wang, M. Yang, K. Du, Z. Fu, D. Kong, D. Dai, Y. Jin, G. Li, H. Li, Q. Peng, J. Wang, W. Huang, Nature 2018, 562, 249; Q. Van Le, H. W. Jang, S. Y. Kim, Small Methods 2018, 2, 1700419; Z. Feng, L. Wang, H. Yu, X. Ma, Q. Zhang, S. Chen, L. Liu, W. Huang, Organic Electronics 2018, 61, 18; R. Kumar, J. Kumar, P. Srivastava, D. Moghe, D. Kabra, M. Bag, ACS Applied Materials & Interfaces 2020, 12, 34265; H. Ji, Z. Shi, X. Sun, Y. Li, S. Li, L. Lei, D. Wu, T. Xu, X. Li, G. Du, ACS Applied Materials & Interfaces 2017, 9, 42893.
[11] Y. Ding, J. Chen, H. Chen, Y. Yang, J. Xu, J. Yao, Applied Surface Science 2020, 510, 145356; H. B. Kim, I. Im, Y. Yoon, S. D. Sung, E. Kim, J. Kim, W. I. Lee, Journal of Materials Chemistry A 2015, 3, 9264.
[12] A. Zohar, M. Kulbak, I. Levine, G. Hodes, A. Kahn, D. Cahen, ACS Energy Letters 2019, 4, 1.
[13] A. Rajagopal, R. J. Stoddard, S. B. Jo, H. W. Hillhouse, A. K. Y. Jen, Nano Letters 2018, 18, 3985.
[14] E. Calabrò, F. Matteocci, B. Paci, L. Cinà, L. Vesce, J. Barichello, A. Generosi, A. Reale, A. Di Carlo, ACS Applied Materials & Interfaces 2020, 12, 32536; J. Qin, J. Zhang, Y. Bai, S. Ma, M. Wang, H. Xu, M. Loyd, Y. Zhan, X. Hou, B. Hu, iScience 2019, 19, 378; J. Wang, J. Zhang, Y. Zhou, H. Liu, Q. Xue, X. Li, C.-C. Chueh, H.-L. Yip, Z. Zhu, A. K. Y. Jen, Nature Communications 2020, 11, 177; S.-Y. Wang, C.-P. Chen, C.-L. Chung, C.-W. Hsu, H.-L. Hsu, T.-H. Wu, J.-Y. Zhuang, C.-J. Chang, H. M. Chen, Y. J. Chang, ACS Applied Materials & Interfaces 2019, 11, 40050; C.-J. Yu, Y.-H. Kye, U.-G. Jong, K.-C. Ri, S.-H. Choe, J.-S. Kim, S.-G. Ko, G.-I. Ryu, B. Kim, ACS Applied Materials & Interfaces 2020, 12, 1858.
[15] Y. H. Lee, J. Luo, M.-K. Son, P. Gao, K. T. Cho, J. Seo, S. M. Zakeeruddin, M. Grätzel, M. K. Nazeeruddin, Advanced Materials 2016, 28, 3966; X. Li, C.-C. Chen, M. Cai, X. Hua, F. Xie, X. Liu, J. Hua, Y.-T. Long, H. Tian, L. Han, Advanced Energy Materials 2018, 8, 1800715; K. Xiao, C. Cui, P. Wang, P. Lin, Y. Qiang, L. Xu, J. Xie, Z. Yang, X. Zhu, X. Yu, D. Yang, Nanotechnology 2018, 29, 065401.
[16] T.-H. Han, J.-W. Lee, C. Choi, S. Tan, C. Lee, Y. Zhao, Z. Dai, N. De Marco, S.-J. Lee, S.-H. Bae, Y. Yuan, H. M. Lee, Y. Huang, Y. Yang, Nature Communications 2019, 10, 520; X. Li, M. Ibrahim Dar, C. Yi, J. Luo, M. Tschumi, S. M. Zakeeruddin, M. K. Nazeeruddin, H. Han, M. Grätzel, Nature Chemistry 2015, 7, 703.
[17] Z. Zhou, Z. Wang, Y. Zhou, S. Pang, D. Wang, H. Xu, Z. Liu, N. P. Padture, G. Cui, Angewandte Chemie International Edition 2015, 54, 9705.
[18] Y. Jiang, E. J. Juarez-Perez, Q. Ge, S. Wang, M. R. Leyden, L. K. Ono, S. R. Raga, J. Hu, Y. Qi, Materials Horizons 2016, 3, 548; M.-J. Zhang, N. Wang, S.-P. Pang, Q. Lv, C.-S. Huang, Z.-M. Zhou, F.-X. Ji, ACS Applied Materials & Interfaces 2016, 8, 31413; S. Pang, Y. Zhou, Z. Wang, M. Yang, A. R. Krause,

Z. Zhou, K. Zhu, N. P. Padture, G. Cui, Journal of the American Chemical Society 2016, 138, 750; Z. Liu, L. Qiu, E. J. Juarez-Perez, Z. Hawash, T. Kim, Y. Jiang, Z. Wu, S. R. Raga, L. K. Ono, S. Liu, Y. Qi, Nature Communications 2018, 9, 3880.
[19] T. Zhang, N. Guo, G. Li, X. Qian, L. Li, Y. Zhao, Journal of Materials Chemistry A 2016, 4, 3245.
[20] S. R. Raga, Y. Jiang, L. K. Ono, Y. Qi, Energy Technology 2017, 5, 1750.
[21] Z. Shao, Z. Wang, Z. Li, Y. Fan, H. Meng, R. Liu, Y. Wang, A. Hagfeldt, G. Cui, S. Pang, Angewandte Chemie International Edition 2019, 58, 5587.
[22] A. Singh, A. S. Chouhan, S. Avasthi, Materials Research Express 2019, 6, 085519.
[23] T. Zhang, G. Li, F. Xu, Y. Wang, N. Guo, X. Qian, Y. Zhao, Chemical Communications 2016, 52, 11080.
[24] K. T. Butler, J. M. Frost, A. Walsh, Materials Horizons 2015, 2, 228.
[25] F. Urbach, Physical Review 1953, 92, 1324.
[26] M. J. Trimpl, A. D. Wright, K. Schutt, L. R. V. Buizza, Z. Wang, M. B. Johnston, H. J. Snaith, P. Müller-Buschbaum, L. M. Herz, Advanced Functional Materials 2020, 30, 2004312.
[27] H. Zhu, Y. Liu, F. T. Eickemeyer, L. Pan, D. Ren, M. A. Ruiz-Preciado, B. Carlsen, B. Yang, X. Dong, Z. Wang, H. Liu, S. Wang, S. M. Zakeeruddin, A. Hagfeldt, M. I. Dar, X. Li, M. Grätzel, Advanced Materials 2020, 32, 1907757.
[28] M. C. Troparevsky, A. S. Sabau, A. R. Lupini, Z. Zhang, Opt. Express 2010, 18, 24715.
[29] M. A. d. Maur, G. Penazzi, G. Romano, F. Sacconi, A. Pecchia, A. D. Carlo, IEEE Transactions on Electron Devices 2011, 58, 1425.
[30] A. Hernández-Granados, A. N. Corpus-Mendoza, P. M. Moreno-Romero, C. A. Rodríguez-Castañeda, J. E. Pascoe-Sussoni, O. A. Castelo-González, E. C. Menchaca-Campos, J. Escorcia-García, H. Hu, Optical Materials 2019, 88, 695.
[31] E. Lamanna, F. Matteocci, E. Calabrò, L. Serenelli, E. Salza, L. Martini, F. Menchini, M. Izzi, A. Agresti, S. Pescetelli, S. Bellani, A. E. Del Río Castillo, F. Bonaccorso, M. Tucci, A. Di Carlo, Joule 2020, 4, 865.
[32] M. V. Khenkin, E. A. Katz, A. Abate, G. Bardizza, J. J. Berry, C. Brabec, F. Brunetti, V. Bulović, Q. Burlingame, A. Di Carlo, R. Cheacharoen, Y.-B. Cheng, A. Colsmann, S. Cros, K. Domanski, M. Dusza, C. J. Fell, S. R. Forrest, Y. Galagan, D. Di Girolamo, M. Grätzel, A. Hagfeldt, E. von Hauff, H. Hoppe, J. Kettle, H. Köbler, M. S. Leite, S. Liu, Y.-L. Loo, J. M. Luther, C.-Q. Ma, M. Madsen, M. Manceau, M. Matheron, M. McGehee, R. Meitzner, M. K. Nazeeruddin, A. F. Nogueira, Ç. Odabaşı, A. Osherov, N.-G. Park, M. O. Reese, F. De Rossi, M. Saliba, U. S. Schubert, H. J. Snaith, S. D. Stranks, W. Tress, P. A. Troshin, V. Turkovic, S. Veenstra, I. Visoly-Fisher, A. Walsh, T. Watson, H. Xie, R. Yıldırım, S. M. Zakeeruddin, K. Zhu, M. Lira-Cantu, Nature Energy 2020, 5, 35.